Electronic Research Archive

http://www.aimspress.com/journal/era

ERA, 30(3): 961–977.
DOI: 10.3934/era.2022050
Received: 28 September 2021
Revised: 07 December 2021
Accepted: 15 December 2021
Published: 04 March 2022

Research article

In-phase and anti-phase spikes synchronization within mixed Bursters of the pre-Bözinger complex

Moutian Liu and Lixia Duan*

College of Science, North China University of Technology, Beijing 100144, China

* **Correspondence:** Email: duanlx@ncut.edu.cn

Abstract: In this paper, the transition from anti-phase spike synchronization to in-phase spike synchronization within mixed bursters is investigated in a two-coupled pre-Bözinger complex (pre-BötC) network. In this two-coupled neuronal network, the communication between two pre-BötC networks is based on electrical and synaptic coupling. The results show that the electrical coupling accelerates in-phase spike synchronization within mixed bursters, but synaptic coupling postpones this kind of synchronization. Synaptic coupling promotes anti-phase spike synchronization when electrical coupling is weak. At the same time, the in-phase spike synchronization within dendritic bursters occurs earlier than that within somatic bursters. Asymmetric periodic somatic bursters appear in the transition state from anti-phase spikes to in-phase spikes. We also use fast/slow decomposition and bifurcation analysis to clarify the dynamic mechanism for the two types of synchronization.

Keywords: in-phase spikes; anti-phase spikes; pre-Bözinger complex; mixed bursters; synchronization

1. Introduction

Neuronal communication is based on synapses, including both chemical and electrical synapses [1, 2]. Electrical synapses are widespread in mammalian brain neural circuits and regulate the firing pattern of interconnected neurons [2, 3]. Electrical synapses can increase neuronal excitability and accelerate the synchronization of neuronal firing [4–6]. Neuronal synchronization makes a valuable contribution toward maintaining some physiological functions of the brain [7]. The synchronization of neuronal networks has been widely studied, mainly focusing on complete, phase, and lag synchronization [8–11]. As for the issues of synchronization transitions between in-phase and anti-phase spikes, some studies have focused on the firing of normal bursters in a neural system [12]. However, the firing of mixed bursters is global in a neural network, and their synchronization seems to be consequential.

There has been considerable research on normal bursters in coupled neurons. Sherman et al. stud-

ied a simplified model for a pair of pancreatic beta cells coupled by electrical synapses, and they analyzed the fast subsystem to illuminate how electrical coupling affects bifurcation behavior. When the coupling is weak, the spikes within bursters are not in-phase, but rather anti-phase, asymmetric, and quasi-periodic [13]. De Vries et al. used a general weakly coupled nonlinear oscillator model to understand the burster mechanism of pancreatic beta cells, and obtained similar results using a more simplified model [14]. Yang et al. analyzed a relatively simple model consisting of two identical coupled layers. The coupling induced new bifurcations, leading to multi-stability. A pair of distinct, unstable, asymmetric steady states were observed [15]. Toporikova et al. showed the effect of synaptic and electrical coupling on burst dynamics and spike synchronization within bursters via the coupled neuronal model pre-Bözinger complex (pre-BötC). Electrical coupling promotes spikes of in-phase synchronization within a burster, and synaptic coupling promotes the transition of anti-phase spikes within bursters [12]. Duan et al. studied the relationship between the in-phase and anti-phase spikes within a mixed burster and the following initial values: the in-phase spike synchronization within a mixed burster corresponded to the same initial values, and the anti-phase spike synchronization corresponded to different initial values [16–18]. The local and global stability of the coupled networks were analyzed and there are also many studies on the stable regions and bifurcation curves of the coupled networks in parameter planes [19]. The codimension-2 bifurcation analysis of neuronal system for mixed-mode oscillations shown more details of bifurcation [20, 21]. However, the transition of the in-phase and anti-phase spike synchronization within the mixed burster was not revealed.

This paper is organized as follows. A modified neuronal model, the coupled pre-BötC model, is introduced in Section 2. In Section 3, we explore how the mixed burster pattern of the system depends on the parameters of both electrical (g_{gap}) and synaptic (g_{syn-e}) coupling. We study how the parameters g_{gap} and g_{syn-e} affect the anti-phase and in-phase spike synchronization of mixed bursters. By fast/slow decomposition and bifurcation analysis, we investigate the dynamic mechanisms of synchronization. We find that the synchronization of spikes within dendritic bursters occurs earlier than within somatic bursters. The transition state between in-phase and anti-phase spike synchronization is called the asymmetric periodic somatic burster. Finally, a discussion is provided in the last section.

2. Model description

The single-compartment pre-BötC inspiratory neurons [22] are coupled and modified as follows:

$$\dot{V}_i = (-I_{NaP_i} - I_{CAN_i} - I_{Na_i} - I_{K_i} - I_{L_i} - I_{syn-e_i} - I_{gap_i})/C, \tag{2.1}$$

where $i, j = 1, 2$ and $i \neq j$, V is the membrane potential; I_{NaP}, I_{CAN}, I_{Na}, I_K, I_L, I_{syn-e}, and I_{gap} represent the persistent sodium current, calcium-activated nonspecific cationic current, Na^+ current, delayed-rectifier K^+ current, leakage current, synaptic coupling current, and electric coupling current, respectively; and C is the overall cell capacitance. These currents are calculated as follows:

$$\begin{aligned}
&I_{NaP_i} = g_{Nap} m p_\infty h_i (V_i - E_{Na}),\\
&I_{CAN_i} = g_{CAN} f([Ca]_i)(V_i - E_{Na}),\\
&I_{Na_i} = g_{Na} m_\infty^3(V_i)(1 - h_i)(V_i - E_{Na}),\\
&I_{K_i} = g_K n_i^3 (V_i - E_K),\\
&I_{L_i} = g_L (V_i - E_L),
\end{aligned}$$

$$I_{syn-e_i} = g_{syn-e} s_i (V_i - E_{syn-e}),$$
$$I_{gap_i} = g_{gap}(V_i - V_j).$$

The activation and inactivation variables n and h are described by the following equations:

$$\dot{n}_i = (n_\infty(V_i) - n_i)/\tau_n(V_i), \tag{2.2}$$

$$\dot{h}_i = (h_\infty(V_i) - h_i)/\tau_h(V_i). \tag{2.3}$$

The voltage-dependent activation and inactivation steady states and the time constants are described as follows:

$$\alpha_\infty(V_i) = \frac{1}{1 + e^{\frac{V_i - \theta_\alpha}{\sigma_\alpha}}}, \qquad \alpha = mp, m, h, n, s$$
$$\tau_\beta(V_i) = \frac{\tau_\beta}{\cosh \frac{V_i - \theta_\beta}{2\sigma_\beta}}. \qquad \beta = n, h$$

The synaptic activation variable s can be described as follows:

$$\dot{s}_i = \alpha_s(1 - s_i)s_\infty(V_j) - s_i/\tau_s. \tag{2.4}$$

The Ca^{2+} kinetics are described by two equations representing the intracellular Ca^{2+} balance ($[Ca]$) and IP3 channel gating variable (l):

$$[\dot{Ca}]_i = f_c(J_{ER_{IN}} - J_{ER_{OUT}}), \tag{2.5}$$

$$\dot{l}_i = AK_d(1 - l_i) - A[Ca]_i l_i. \tag{2.6}$$

The flux into the cytosol from the ER ($J_{ER_{IN}}$) and the flux from the cytosol back to the ER ($J_{ER_{OUT}}$) are described as follows:

$$J_{ER_{IN}} = [L_{IP3} + P_{IP3}(\frac{[IP3][Ca]_i l_i}{([IP3] + K_I)([Ca]_i + K_a)})^3](\frac{[Ca]_{Tot} - [Ca]_i}{\sigma} - [Ca]_i l_i),$$
$$J_{ER_{OUT}} = V_{SERCA}\frac{[Ca]_i^2}{K_{SERCA}^2 + [Ca]_i^2}.$$

The function $f([Ca]_i)$ describes the activation of I_{CAN} by Ca^{2+}:

$$f([Ca]_i) = \frac{1}{1 + \frac{[K_{CAN}]^{n_{CAN}}}{[Ca]_i}},$$

The parameter values used in the model are listed in Table 1.

The function of the coupled neuron spike phase is as follows:

$$\phi_i = 2k\pi + 2\pi\frac{t - t_i^k}{t_i^{k+1} - t_i^k}, (t_i^k < t < t_i^{k+1}, k = 1, 2, ...N - 1), (i, j = 1, 2),$$

where t represents time, t_i^k is the time when the k-th spike fires in the i-th neuron, and N is the number of spikes. The phase difference of a spike is defined as follows:

$$\Delta\phi(t) = |\phi_1(t) - \phi_2(t)|.$$

According to the values of $\max(\Delta\phi(t))$, we define the synchronization of spikes within mixed bursters as follows:

Table 1. Values of parameters in the model.

Parameter	Value	Parameter	Value	Parameter	Value
θ_{mp}	−40 mV	τ_h	10000 ms	E_L	−58 mV
θ_m	−34 mV	τ_n	100 ms	E_{syn-e}	0 mV
θ_h	−48 mV	τ_s	5 ms	n_{CAN}	0.97
θ_n	−29 mV	g_{NaP}	3 nS	K_{CAN}	0.74 μM
θ_s	−10 mV	g_{Na}	15 nS	$[Ca]_{Tot}$	1.25 μM
σ_{mp}	−6 mV	g_K	9 nS	σ	0.185
σ_m	−5 mV	g_L	2.3 nS	V_{SRECA}	400
σ_h	5 mV	g_{CAN}	0.7 nS	k_{SRECA}	0.2 μM
σ_n	−4 mV	E_{Na}	50 mV	L_{IP3}	0.27 pL $\cdot$ s^{-1}
σ_s	−5 mV	E_K	−85 mV	P_{IP3}	31000 pL $\cdot$ s^{-1}
K_I	1.0 μM	K_a	0.4 μM	$[IP_3]$	0.95 μM
C	21 μF	α_s	0.2	f_c	0.000025 pL^{-1}
A	0.001 μM^{-1} $\cdot$ s^{-1}	K_d	0.4 μM		

(a) $\max(\Delta\phi(t)) = 0$: In-phase synchronization of a spike;

(b) $\max(\Delta\phi(t)) = \pi$: Anti-phase synchronization of a spike;

(c) $0 < \max(\Delta\phi(t)) < \pi$: Out of phase synchronization of a spike.

(d) $\max(\Delta\phi(t)) > \pi$: Asynchronization of a spike.

Our mathematical model of coupled pre-BötC involves two independent burster mechanisms. Bursters in the somatic compartment are modeled via the inactivation of a persistent sodium current(I_{NaP}) in the Eq (2.1), whereas bursters in the dendritic compartment rely on Ca^{2+} oscillations, which are determined by the neuromodulatory tone and modeled via calcium-activated nonspecific cationic current (I_{CAN}) in the Eq (2.1). The former are usually called somatic bursters, and the latter are called dendritic bursters (Figure 1(e)).

3. Results

3.1. Effects of electrical and synaptic coupling strength on mixed bursters

To investigate the effects of the electrical and synaptic coupling strength on mixed bursters, we use the interspike interval (ISI) of the membrane potential V_1 to describe the variations of the mixed burster pattern. The ISIs when varying g_{syn-e} with different fixed values of g_{gap} are shown Figure 1(a)–(d). The ISI sequences can be divided into four types, as shown in Figure 1(a) (refer to Figure 1(f) for details). These types are described as follows:

Type 1 (refer to marker d_1 in Figure 1(f)): the top wavy sequences. The interspike interval is from the start of the last spike of the dendritic burster in the previous period to the first spike of the first somatic burster in the next period.

Type 2 (refer to marker d_2 in Figure 1(f)): the second lasting increasing linear sequence. The interval is between two adjacent somatic bursters.

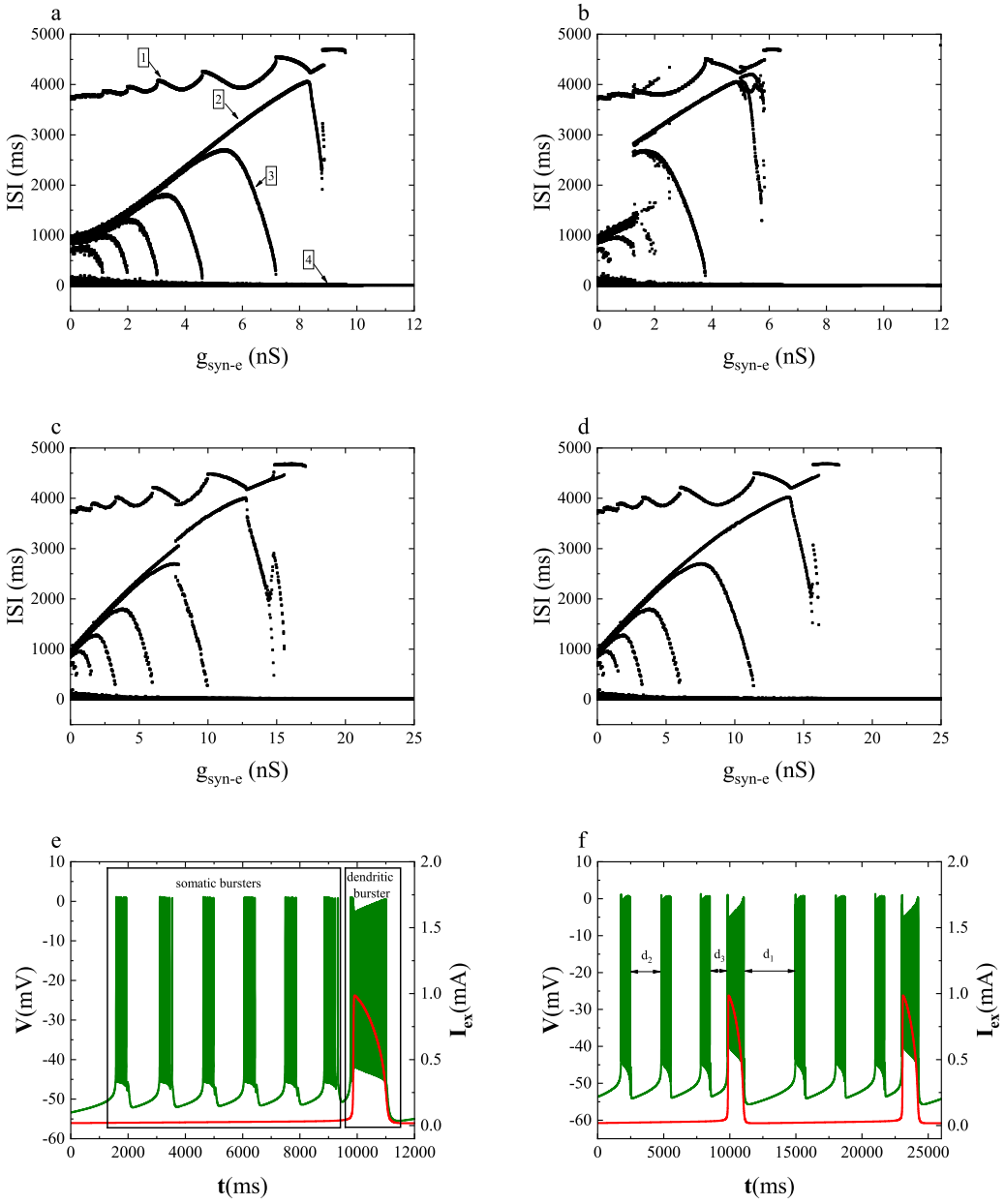

Figure 1. Interspike interval (ISI) diagrams for the parameter g_{syn-e} with different values of g_{gap}: (a) $g_{gap} = 0$ (nS), (b) $g_{gap} = 1$ (nS), (c) $g_{gap} = 2$ (nS), and (d) $g_{gap} = 3$ (nS). Time sequences with g_{gap} fixed at 1 nS: (e) $g_{syn-e} = 1$ (nS) and (f) $g_{syn-e} = 4$ (nS). The olive and red curves represent V_1 and $[Ca]$, respectively. Type 1 (d_1): Interval between the dendritic burster and the next somatic burster. Type 2 (d_2): Interval between the adjacent somatic bursters. Type 3 (d_3): Interval between the dendritic burster and the previous somatic burster. Type 4: Interspike interval within bursters.

Type 3 (refer to marker d_3 in Figure 1(f)): the parabolic sequences. The interval is between the last somatic burster and dendritic burster in one period.

Type 4: the bottom sequences. The interspike intervals are within bursters.

For $g_{gap} = 0$ (nS), with the increase in g_{syn-e}, d_1 is slowly increases in general. d_2 increases approximately linearly, which indicates that the intervals between two adjacent somatic bursters increase accordingly. The trend of d_3 is parabolic and periodic. Every parabolic sequence starts at the sequences of d_2 and ends at the sequences of d_4, which means that the last somatic burster approaches a dendritic burster, and then they merge with each other. The number of parabolic sequences is the number of somatic bursters in one period. In summary, with the increase in g_{syn-e}, the number of somatic bursters gradually decreases to 0. The somatic bursters then finally transition to spike firing. The ISI diagrams with $g_{gap} = 1$, 2, and 3 (nS) are shown in Figure 1(b), (c), and (d), respectively. The structure of the ISI diagrams with different g_{gap} is similar to that shown in Figure 1(a). As the parameter g_{gap} increases, the value of g_{syn-e}, which transitions to spike firing, increases correspondingly.

With a fixed g_{syn-e}, the ISI diagrams with $g_{syn-e} = 0$, 2, 4, and 6 (nS) are shown in Figure 2. When g_{syn-e} is 0 nS (Figure 2(a)), with the increase in g_{gap}, the ISIs begin to increase initially, similar to the behavior shown in Figure 1(a)–(d). In particular, the number of somatic busters decreasing. When g_{gap} reaches a critical value, the ISIs remain unchanged, regardless of how g_{gap} increases. This critical value signifies that the mixed bursters reach a steady state in which the time sequences maintain the same pattern. When g_{syn-e} increases to 2 nS, the critical value increases correspondingly (Figure 2(b)). With g_{syn-e} increasing to 4 nS, the former part of the ISI is also increasing as g_{gap} increases, and the critical value also increases. There seems to be a transition state before the ISIs reach the steady state (Figure 2(c)). When g_{syn-e} increases to 6 nS, the region of the transition state and critical value also increase correspondingly (Figure 2(d)).

3.2. In-phase and anti-phase spike synchronization within somatic bursters

We select the first somatic burster of periodic mixed bursters to investigate its synchronization. In Section 3.1, we found that there is a steady state of ISIs with a change in g_{syn-e} or g_{gap}. With the increase in the value of g_{gap}, the somatic burster of the coupled system transitions to complete spike synchronization from anti-phase spikes, as shown in Figure 3. For $g_{gap} = 0.2$ (nS), the spikes within a somatic burster are almost anti-phase, as shown in Figure 3(a). With g_{gap} increasing to 0.6 nS, the duration of the somatic burster increases, and the first several spikes begin to be in-phase, while others are still anti-phase within one somatic burster, as shown in Figure 3(b). When g_{gap} increases to 1.3 nS, all the spikes within the somatic burster remain in-phase (Figure 3(c)). When g_{gap} further increases to 2 nS, the spikes within the somatic burster still stay in the in-phase state and maintain the same firing pattern, for example, as shown in Figure 3(d). Compared with the cases considered in Section 3.1, increasing g_{gap} leads to in-phase spike synchronization for the somatic bursters. Furthermore, g_{gap} will not affect the state of the coupled system when g_{gap} is greater than a critical value. However, increasing g_{syn-e} will delay the synchronization, because increasing g_{syn-e} leads to an increase in the critical value (shown in Figure 2).

As we mentioned earlier, the increase in g_{gap} leads to a critical value at which the coupled system transitions to in-phase spikes from anti-phase spikes, and the increase in g_{syn-e} postpones the critical value. To better understand the influence of the two kinds of coupling strengths on the critical value, we record the average values of the phase difference of the spikes in somatic bursters with the parameters

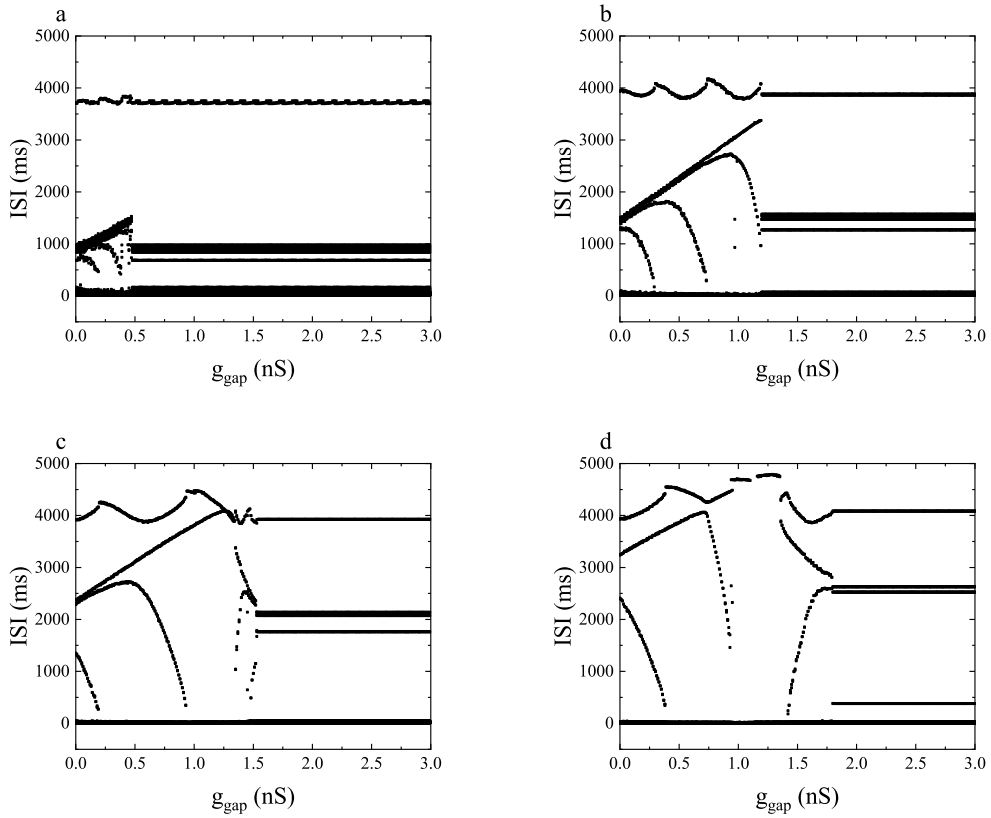

Figure 2. ISI diagrams for a fixed value of parameter g_{gap} with different values of g_{syn-e}: (a) g_{syn-e} = 0 (nS), (b) g_{syn-e} = 2 (nS), (c) g_{syn-e} = 4 (nS), and (d) g_{syn-e} = 6 (nS).

g_{gap} and g_{syn-e}. The pseudo-color diagram in the (g_{gap}, g_{syn-e})-plane is shown in Figure 4. The color represents the average values of the phase difference of the spikes, and the number represented by the color is shown in the colormap on the right. There is a distinct boundary between the in-phase and anti-phase spike synchronization regions. With the increase in g_{syn-e}, the boundary moves to the direction in which g_{gap} is also increasing. The boundary curve is the critical value of the in-phase and anti-phase synchronization in the coupled system. Increasing g_{gap} can indeed lead to the in-phase synchronization of the coupled system, but increasing g_{syn-e} can delay the synchronization through the trend of the boundary curve. For a smaller value of g_{gap}, the system is in anti-phase spike synchronization. Increasing g_{syn-e} will destroy the state in which the somatic burster is in-phase spike synchronization. For a larger value of g_{gap}, the system is in in-phase spike synchronization. As long as g_{gap} is large enough (larger than the synchronization threshold), the system will achieve complete synchronization. When g_{gap} and g_{syn-e} are both small, the synchronization state of the coupled system is affected by both of them. As long as g_{gap} is large enough, g_{gap} will dominate the synchronization state of the coupled system.

Bursters occur within the region of bistability, where both periodic and equilibrium solutions coexist. The region of bistability is necessary for the existence of square-wave bursters [23], as shown in Figure 5. Using h as the bifurcation parameter of the fast subsystem, we explain the dynamic bifurcation mechanisms of the in-phase and anti-phase spike synchronization within somatic bursters for the

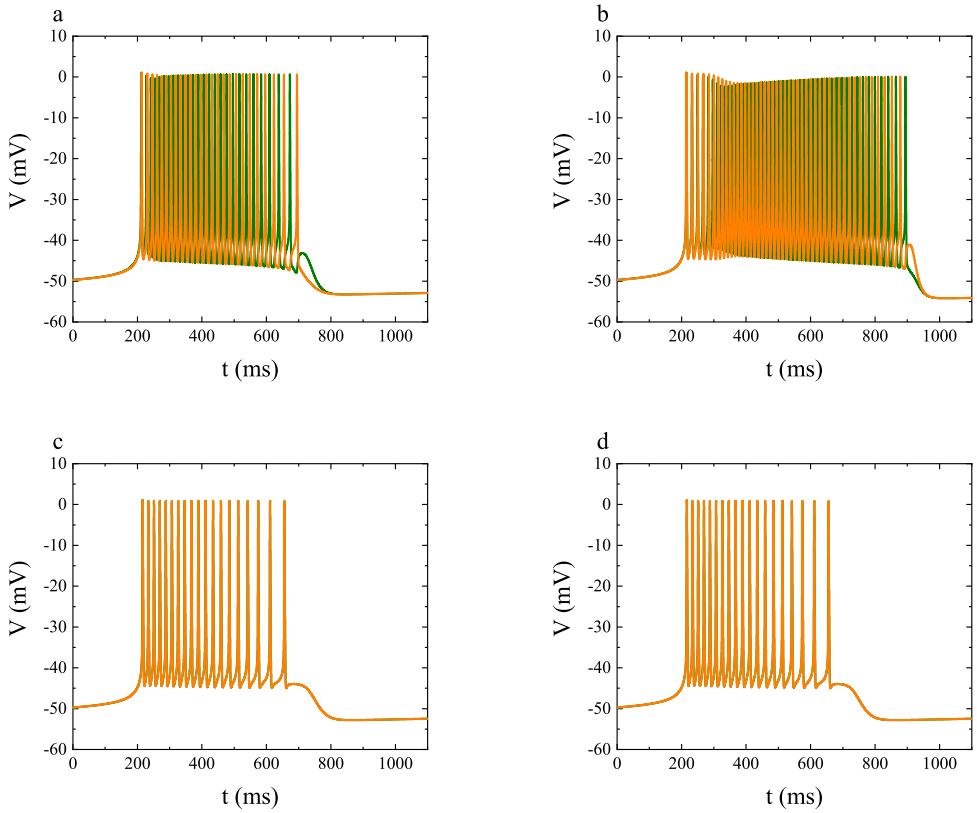

Figure 3. Time sequence of somatic bursters with the increase in g_{gap}: (a) $g_{gap} = 0.2$ (nS), (b) $g_{gap} = 0.6$ (nS), (c) $g_{gap} = 1.3$ (nS), and (d) $g_{gap} = 2$ (nS). g_{syn-e} is fixed at 2 nS. The olive and orange curves represent the membrane potentials V_1 and V_2, respectively.

coupled system. The bifurcation diagrams of the fast subsystem for four different cases (Figure 3) are plotted in Figure 5. The red curve represents an anti-phase periodic solution, which is called the AP branch. The blue curve represents an in-phase periodic solution, which is called the IP branch. The IP branch starts from the IP Hopf bifurcation point and ends at a homoclinic point (HC). The AP branch starts from the AP Hopf bifurcation point. The AP branch is initially unstable but becomes stable through a branch point of cycles (BPC_{AP}), after which it loses its stability through a fold limit bifurcation of cycles (LPC_{AP}). The IP branch is initially unstable, but becomes stable through a fold limit bifurcation of cycles (LPC_{IP}), and then it loses its stability through a branch point of cycles (BPC_{IP}).

The AP branch is stable, but the IP branch is unstable in the bistable region. Thus, the somatic burster contains anti-phase spikes rather than in-phase spikes (Figure 5(a)). When g_{gap} increases to 0.6 nS, as shown in Figure 5(b), although the bistable region still includes a stable AP branch, the spikes within the somatic burster are also anti-phase spikes. Compared with the case in Figure 5(a), BPC_{AP} and BPC_{IP} are shifted to the left along the corresponding branches, which gives rise to a decrease in the size of the stable region of the limit cycle on the AP branch but an increase on the IP branch. With the increase in g_{gap}, the AP branch gradually loses stability and the IP branch gradually obtains a more stable branch through BPC_{AP} and BPC_{IP}, respectively, as shown in Figure 5(a)–(d). When the AP branch loses stability in the whole bistable region, the IP branch will become stable in the bistable

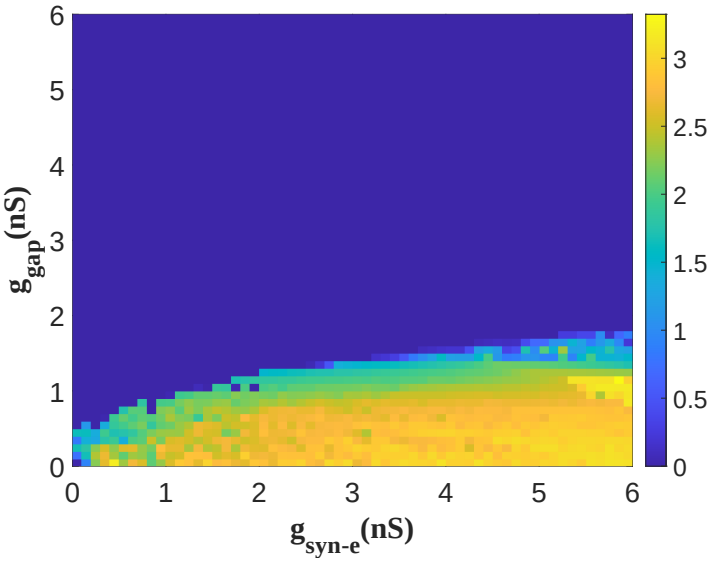

Figure 4. Pseudo-color diagram for in-phase and anti-phase spike synchronization with parameters g_{gap} and g_{syn-e}. The color represents the average value of the phase difference of the spikes. The blue region represents in-phase spike synchronization (the average value of the phase difference is 0) and the yellow region represents anti-phase spike synchronization (the average value of the phase difference is π).

region, as shown in Figure 5(c). The coupled system will enter an in-phase spike state. At the same time, BPC_{IP} will disappear. If g_{gap} continues to increase, the AP branch completely loses stability and BPC_{AP} disappears, as shown in Figure 5(d). However, the IP branch remains stable. The somatic bursters remain in in-phase spike synchronization. At the same time, the increase in g_{gap} causes the AP Hopf bifurcation point to move to the left, along with the AP branch.

The somatic burster in which spikes are anti-phase begins at SN and ends at the LPC_{AP} bifurcation on the AP branch (shown in Figure 5(a) and (b)). The somatic burster in which spikes are in-phase also begins at SN but ends at the HC bifurcation on the IP branch (shown in Figure 5(c) and (d)). BPC_{AP} and BPC_{IP} are heavily related to the anti-phase and in-phase spike synchronizations. Thus, we divide the (h, V) plane into regions I and II by BPC_{AP} and BPC_{IP}, as shown in Figure 6(a). In region I, the IP branch is stable, so it must be related to the in-phase solution. In region II, the AP branch is stable, so it must be related to the anti-phase solution (Figure 6(a)).

The two-parameter bifurcation diagram with parameters h and g_{gap} is shown in Figure 6(b). The somatic burster in which spikes are in-phase begins at SN and ends at HC, and the in-phase solution is stable on the right side of BPC_{IP}. Thus, the curves of SN, HC, and BPC_{IP} form region I, where we select the right side of the curve of BPC_{IP}. In region I, the coupled system exhibits in-phase spikes within somatic bursters. The somatic burster in which spikes are anti-phase also begins at SN but ends at LPC_{AP}. The anti-phase solution is stable on the left side of BPC_{AP}, so the curves of SN, LPC_{AP}, and BPC_{AP} form region II, where we select the left side of the curve of BPC_{AP}. In region II, the coupled system exhibits anti-phase spikes within somatic bursters.

With the increase in g_{gap}, the curves of the AP Hopf bifurcation point, BPC_{IP}, BPC_{AP}, and LPC_{AP},

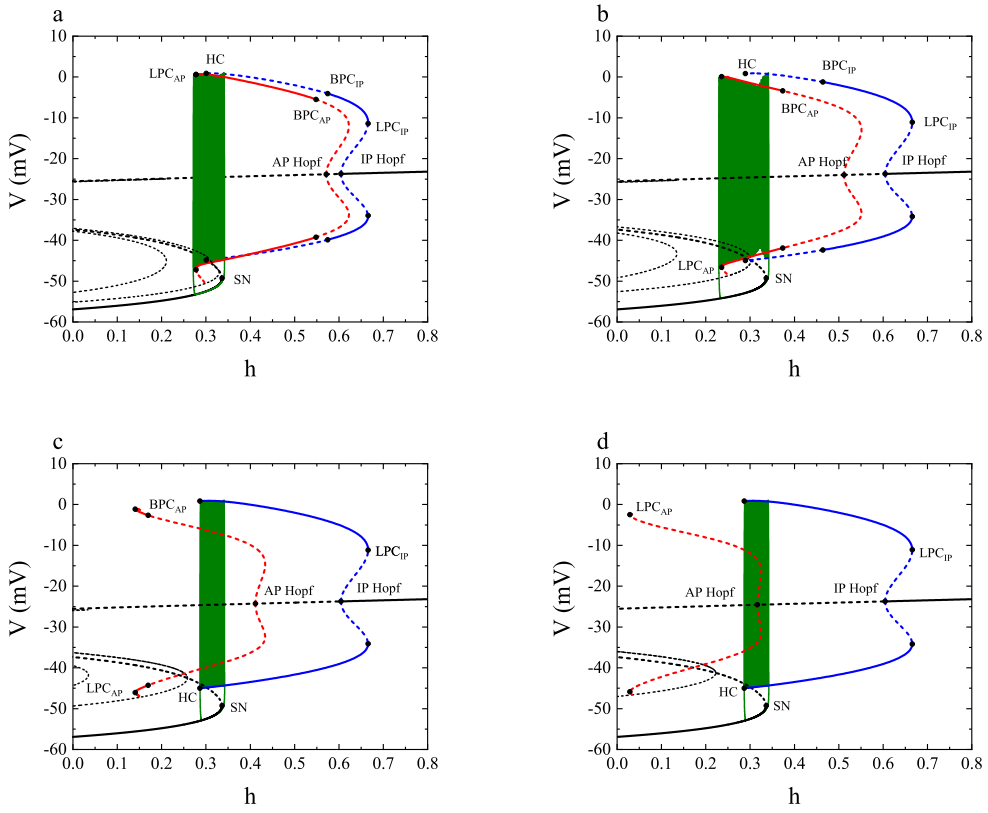

Figure 5. Bifurcation diagrams of fast subsystem with respect to the slow variable parameter h. The dashed and solid lines represent unsteady and steady states, respectively. The red line represents the anti-phase periodic solution, and the blue line represents the in-phase periodic solution, with g_{syn-e} = 2 (nS): (a) g_{gap} = 0.2 (nS), (b) g_{gap} = 0.6 (nS), (c) g_{gap} = 1.3 (nS), and (d) g_{gap} = 2 (nS). AP: Anti-phase periodic solution; IP: In-phase periodic solution; SN: Limit point bifurcation; HC: Homoclinic point bifurcation; LPC: Limit point bifurcation of cycles; BPC: Branch point of cycles.

shift to the left. However, the curves of SN, HC, and the IP Hopf bifurcation point remain unchanged. More specifically, when g_{gap} is roughly equivalent to 1.3 nS, the curve of BPC_{IP} finally merges with the curve of HC, which implies that BPC_{IP} finally falls into the point of HC. As g_{gap} continues to increase, the curve of BPC_{AP} finally merges with the curve of LPC_{AP}, which means that BPC_{AP} finally falls into the point of LPC_{AP}. If g_{gap} is less than 1.3 nS, the trajectory of the coupled system must be located in region II, and the somatic bursters must be anti-phase spikes, such as the cases in Figure 5(a) and (b). When g_{gap} is up to 1.3 nS, the trajectory of coupled system is located in region I, and BPC_{IP} has disappeared but BPC_{AP} has not. The somatic bursters are in-phase spikes, as shown in Figure 5(c). If g_{gap} continues to increase, the trajectory of the coupled system is still located in region I, and the somatic bursters are still in-phase spikes. However, BPC_{AP} gradually merges with LPC_{AP} and disappears, as shown in Figure 5(d).

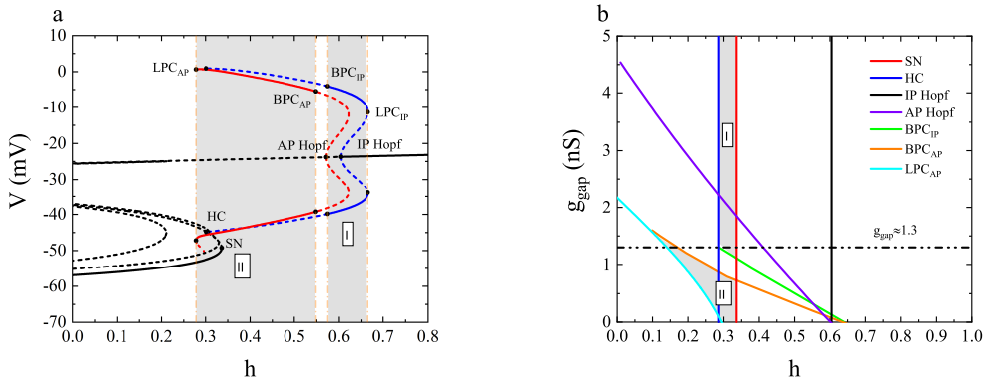

Figure 6. (a): Bifurcation diagram of fast subsystem with g_{syn-e} set to 2 nS. (b): Two-parameter bifurcation diagram of fast subsystem with g_{syn-e} set to 0.2 nS. Region I: In-phase solution; region II: Anti-phase solution.

3.3. Synchronization of spikes within dendritic bursters occurs before that within somatic bursters

In Section 3.2, we discussed the synchronization of spikes in the somatic bursters. The synchronization of dendritic bursters in mixed bursters should be also considered. We next select a period to investigate the synchronization of somatic and dendritic bursters. The phase difference sequences for one period are shown in Figure 7. When g_{gap} is 0.2 nS, the first four columns of $\Delta\phi(t)$ show the phase differences for four somatic bursters, and the last column shows the phase difference for a dendritic burster, as shown in Figure 7(a). $\Delta\phi(t)$ of the somatic bursters is π. However, not all the values of $\Delta\phi(t)$ for the dendritic burster are π. Some were less than π and greater than 0. This implies that the somatic bursters are in the anti-phase spike state, and that the former part of the dendritic burster has started to transition from anti-phase spikes to in-phase spikes. As g_{gap} increases to 0.7 nS, the somatic bursters still remain in the anti-phase spike state. However, the dendritic burster almost reaches in-phase spike synchronization, because $\Delta\phi(t)$ is close to zero except a little part of it, as shown in Figure 7(b). As g_{gap} continues to increase, the somatic bursters have started to transition from anti-phase spikes to in-phase spikes, and the dendritic burster has almost reached in-phase spike synchronization (Figure 7(c)). When g_{gap} is 1.3 nS, $\Delta\phi(t)$ remains at zero during one period (Figure 7(d)), and all the bursters reach in-phase synchronization. Based on the phase difference sequences for one period, we conclude that the time at which spike synchronization occurs within the dendritic bursters is earlier than that within the somatic bursters.

With $[Ca]_{tot} = g_{CAN} f([Ca])$ [22] set as the slow parameter, we perform the bifurcation analysis to explain why in-phase spike synchronization within dendritic bursters occurs earlier than within somatic bursters. The abrupt increase in $[Ca]_{tot}$ leads to the beginning of the dendritic burster, and the gating variable h that originally increases also decreases, as shown in Figure 8(a). When h decreases to the lowest point, it begins to increase, and the dendritic burster ends. The parameters are the same as those in Figure 7(b), so the dendritic burster is in-phase but the somatic bursters are not. With the increase in $[Ca]_{tot}$, the bifurcation points of SN, HC, $\mathrm{BPC_{IP}}$, $\mathrm{LPC_{AP}}$, and $\mathrm{BPC_{AP}}$ move in the direction of h decreasing, as shown in Figure 8(b). As described above, the anti-phase solution begins at SN and ends at $\mathrm{LPC_{AP}}$, and the anti-phase solution is stable on the left side of $\mathrm{BPC_{AP}}$. Thus, there must

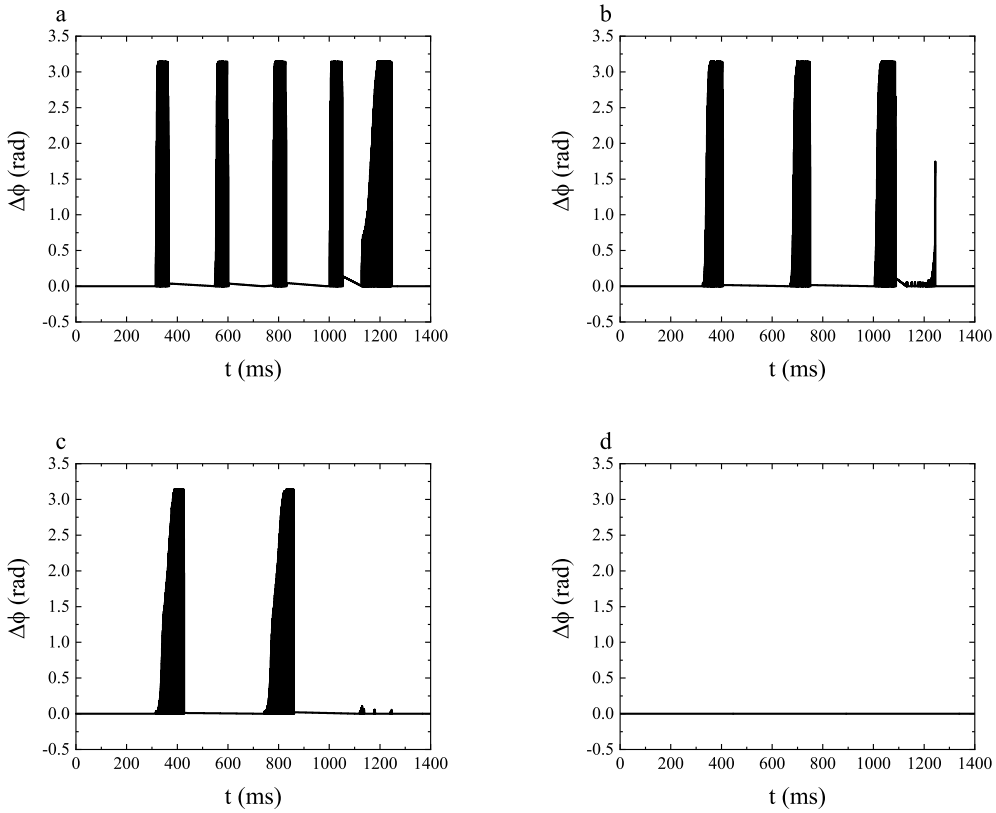

Figure 7. Phase difference sequences for one complete period with g_{syn-e} fixed at 2 nS: (a) g_{gap} = 0.2 (nS), (b) g_{gap} = 0.7 (nS), (c) g_{gap} = 1 (nS), and (d) g_{gap} = 1.3 (nS).

be an anti-phase solution in region II. The in-phase solution is stable on the right side of BPC_{IP}, so there must be an in-phase solution in region I. The trajectory of the somatic bursters lies between the curves LPC_{AP} and SN in region II. This means that the somatic bursters are anti-phase spikes. When $[Ca]_{tot}$ increases to about 0.4 nS, the dendritic burster appears, and the trajectory is only in region I, which indicates that the dendritic burster is in an in-phase spike state. The beginning of h increasing corresponds to the end of the dendritic burster. However, before the end of the dendritic burster, a small part of the trajectory falls in region II, which explains why a small part of the dendritic burster is in an anti-phase spike state (Figure 8(b)). The rapid jump of $[Ca]_{tot}$ caused the trajectory to transition from region II to region I, which is the reason that the synchronization of in-phase spikes within the dendritic bursters occurs earlier than within the somatic bursters.

3.4. Transition between in-phase and anti-phase spike synchronization: asymmetric periodic somatic bursters

The somatic bursters transition from anti-phase spikes to in-phase spikes, then they change into asymmetric periodic somatic bursters. The amplitude of the somatic burster for V_1 is not the same as that for V_2, as shown in Figures 9(a) and (b). The amplitude of the first somatic burster (V_1) in Figure 9(a) is smaller than that of the first somatic burster (V_2) in Figure 9(b). However, the result is opposite for the second somatic burster. At the same time, it should be noted that the type of the first

somatic burster for V_1 is the same as that of the second somatic burster for V_2, and that the type of second somatic burster for V_1 is the same as that of the first somatic burster for V_2.

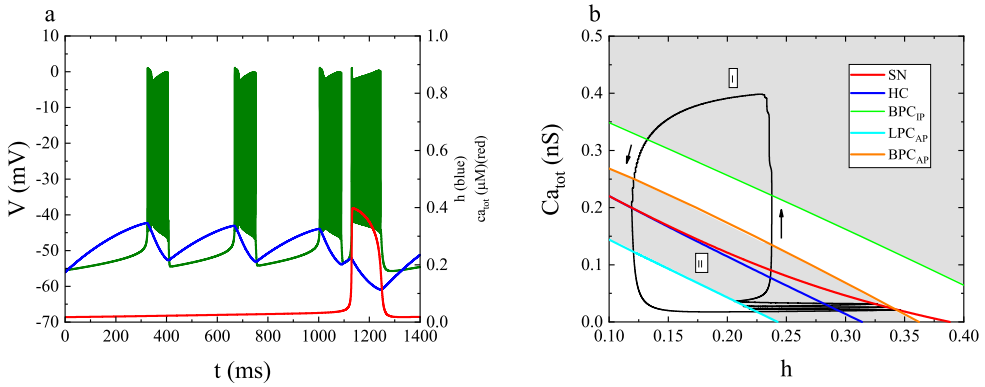

Figure 8. (a) Time sequence diagram of V, h, and $[Ca]_{tot}$. The olive curve represents V, the blue curve represents h, and the red curve represents $[Ca]_{tot}$. (b) Two-parameter bifurcation diagram of the curves of SN, HC, BPC_{IP}, LPC_{AP}, and BPC_{AP}, where g_{syn-e} is 2 nS and g_{gap} is 0.7 nS, region I: In-phase solution; region II: Anti-phase solution.

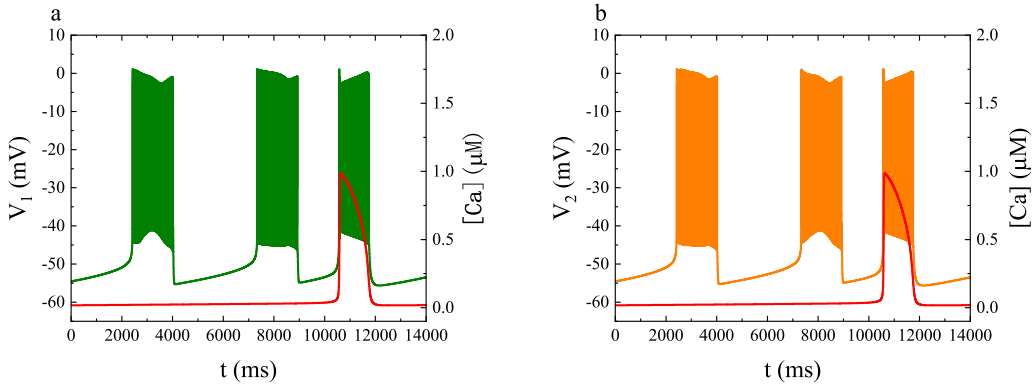

Figure 9. Time sequence diagrams for asymmetric periodic somatic bursters, where g_{syn-e} is 2 nS and g_{gap} is 1.15 nS. The olive curve represents V, and the red curve represents $[Ca]$.

Using fast/slow decomposition and bifurcation analysis, we analyze the asymmetric periodic somatic bursters in Figures 9(a) and (b). By extending BPC_{IP}, we obtain two new pairs of stable branches that start at BPC_{IP} and end at BPC_{AP}, as shown in Figure 10(a) and (b). The violet and cyan curves represent maximum and minimum values of the stable limit cycles. The branch with a smaller amplitude (violet curve) is denoted as the s-ASP branch, and the branch with a larger amplitude (cyan curve) is denoted as the g-ASP branch.

We select the first somatic bursters of V_1 and V_2 in Figure 9(a) and (b) to analyze the dynamic bifurcation mechanisms of the asymmetric periodic somatic bursters. For the first somatic burster of V_1, the asymmetric burster starts at SN and moves to the left along the stable s-ASP branch. It continues to move to the left along the stable AP branch when it passes through BPC_{AP}. The asymmetric burster terminates at LPC_{AP}, which is same behavior as that of the bursters in which spikes are anti-phase, as

shown in Figure 10(a). The asymmetric burster for the first somatic burster of V_2 also starts at SN and then moves to the left along the stable g-ASP branch. It continues to move to the left along the stable AP branch when it passes through BPC_{AP}. The asymmetric burster terminates at LPC_{AP}, as does the burster in which spikes are anti-phase, as shown in Figure 10(b). This results in asymmetric periodic somatic bursters. Based on the above analysis, we infer that the mechanisms for the second somatic burster of V_1 are same as that for the first somatic burster of V_2, and the mechanisms for the second somatic burster of V_2 are same as those for the first somatic burster of V_1.

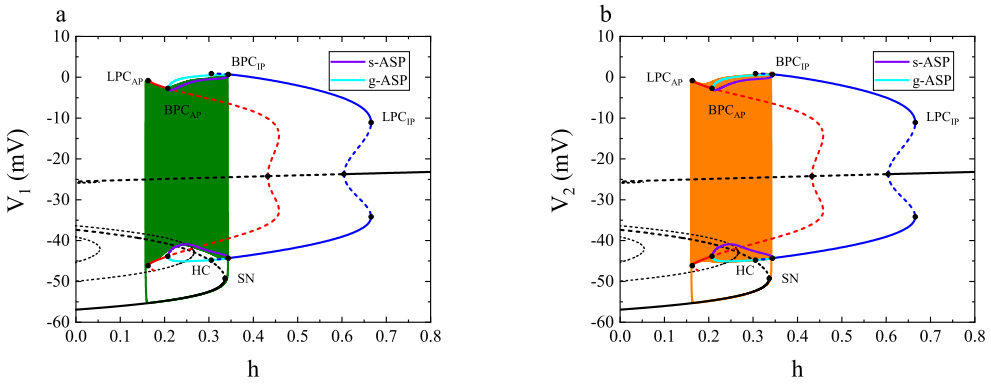

Figure 10. Bifurcation diagrams of the fast subsystem for the first asymmetric periodic somatic burster in Figures 9 (a) and (b).

4. Discussion

We have shown the effects of the electrical and synaptic coupling strength on the in-phase and anti-phase spikes within mixed bursters in the coupled neuronal system of the pre-BötC model. The results show that increasing the electrical coupling accelerates the synchronization of in-phase spikes and changes the number of somatic bursters for mixed bursters in one period. Increasing the synaptic coupling delays the synchronization of in-phase spikes and changes the number of somatic bursters for mixed bursters in one period at the same time. Using fast/slow and bifurcation analysis methods, we analyze the dynamic mechanisms of the in-phase and anti-phase solutions for the coupled system. The in-phase spike synchronization within mixed bursters is largely mediated by the stability of the AP branch. Increasing the electrical coupling leads to movement of BPC_{IP}, causing the IP branch to lose stability. The result is similar to that of anti-phase spikes within mixed bursters. This leads to the bistable region, which consists of a stable AP branch and stable equilibrium points, changing into one that consists of a stable IP branch and stable equilibrium points. Correspondingly, the mixed bursters of the anti-phase spikes turn into the ones of in-phase spikes. Based on this result, we investigate the influence of the second bifurcation parameter g_{gap} on some key bifurcation points. According to the bifurcation mechanisms of the IP and AP branches, the two-parameter bifurcation plane is divided into in-phase and anti-phase solution regions. With the increase in parameter g_{gap}, the trajectory of the coupled system transitions from an anti-phase solution region to an in-phase solution region. The in-phase spike synchronization of the dendritic bursters occurs earlier than that of the somatic bursters.

The oscillation of intracellular Ca^{2+} concentration in the dendrite gives rise to dendritic bursters.

At the same time, the oscillation of intracellular Ca^{2+} causes the trajectory of the system to enter the region in which the solution is in-phase in advance, after which it transitions into the region in which the solution is anti-phase with the decrease in the oscillation of the intracellular Ca^{2+} concentration. The calcium-activated nonspecific cationic current keeps a lower value when the firing pattern of neurons is a somatic burster pattern. For dendritic bursters, the calcium-activated nonspecific cationic current abruptly increases. Therefore, we conclude that the calcium-activated nonspecific cationic current could facilitate the in-phase spike synchronization for mixed bursters.

Our simulations also show that increasing the strength of the electrical coupling from a lower value (corresponding to in-phase spikes) to a higher value (corresponding to anti-phases spikes) causes a transition solution (asymmetric periodic somatic bursters). The IP branch is initially stable, but loses its stability through BPC_{IP}. The bifurcation point of BPC_{IP} gives rise to two new pairs of stable periodic branches. This leads to different dynamic mechanisms for the in-phase and bursters in which spikes are anti-phase. The AP branch is initially unstable, but becomes stable by BPC_{AP}. By coincidence, these two pairs of branches end up at BPC_{AP}. This explains why the asymmetric periodic solution is produced in the transition process between in-phase and anti-phase spikes.

Acknowledgments

This work is supported by the National Natural Science Foundation of China (Grant No. 11872003) and North China University of Technology Research Fund Program for Key Discipline (No. 110052972027/014). The authors are grateful to all the reviewers for their constructive comments.

Conflict of interest

There is no conflicts of interest in this paper.

References

1. A. E. Pereda, Electrical synapses and their functional interactions with chemical synapses, *Nature Rev. Neurosci.*, **15** (2014), 250–263. https://doi.org/10.1038/nrn3708
2. M. V. Bennett, R. S. Zukin, Electrical coupling and neuronal synchronization in the mammalian brain, *Neuron*, **41** (2004), 495–511. https://doi.org/10.1016/S0896-6273(04)00043-1
3. B. W. Connors, M. A. Long, Electrical synapses in the mammalian brain, *Annu. Rev. Neurosci.*, **27** (2004), 393–418. https://doi.org/10.1146/annurev.neuro.26.041002.131128
4. S. Curti, G. Hoge, J. I. Nagy, Synergy between electrical coupling and membrane properties promotes strong synchronization of neurons of the mesencephalic trigeminal nucleus, *J. Neurosci.*, **32** (2012), 4341–4359. https://doi.org/10.1523/JNEUROSCI.6216-11.2012
5. P. A. Getting, Modification of neuron properties by electrotonic synapses. I. Input resistance, time constant, and integration, *J. Neurophysiol.*, **37** (1974), 846–857. https://doi.org/10.1152/jn.1974.37.5.846
6. M. Galarreta, S. Hestrin, Spike transmission and synchrony detection in networks of GABAergic interneurons, *Science*, **292** (2001), 2295–2299. https://doi.org/10.1126/science.1061395

7. D. H. Mathalon,, V. S. Sohal, Neural oscillations and synchrony in brain dysfunction and neuropsychiatric disorders: it's about time, *JAMA Psychiatry*, **72** (2015), 840–844. https://doi.org/10.1001/jamapsychiatry.2015.0483
8. S. Rakshit, B. K. Bera, D. Ghosh, Synchronization in a temporal multiplex neuronal hypernetwork, *Phys. Rev. E*, **98** (2018), 032305. https://doi.org/10.1103/PhysRevE.98.032305
9. Q. Wang, M. Perc, Z. Duan, G. Chen, Synchronization transitions on scale-free neuronal networks due to finite information transmission delays, *Phys. Rev. E*, **80** (2009), 026206. https://doi.org/10.1103/PhysRevE.80.026206
10. M. Jalili, Spike phase synchronization in multiplex cortical neural networks, *Physica A*, **466** (2017), 325–333. https://doi.org/10.1016/j.physa.2016.09.030
11. M. Shafiei, S. Jafari, F. Parastesh, Time delayed chemical synapses and synchronization in multilayer neuronal networks with ephaptic inter-layer coupling, *Commun. Nonlinear Sci. Numer. Simul.*, **84** (2020), 105175. https://doi.org/10.1016/j.cnsns.2020.105175
12. N. Toporikova, T. H. Tsao, T. M. Wright, Conflicting effects of excitatory synaptic and electric coupling on the dynamics of square-wave bursters, *J. Comput. Neurosci.*, **31** (2011), 701–711. https://doi.org/10.1007/s10827-011-0340-1
13. A. Sherman, Anti-phase, asymmetric and aperiodic oscillations in excitable cells—I. Coupled bursters, *Bull. Math. Biol.*, **56** (1994), 811–835. https://doi.org/10.1016/S0092-8240(05)80292-7
14. G. D. Vries, A. Sherman, H. R. Zhu, Diffusively coupled bursters: effects of cell heterogeneity, *Bull. Math. Biol.*, **60** (1998), 1167–1200. https://doi.org/10.1006/bulm.1998.0057
15. L. Yang, I. R. Epstein, Symmetric, asymmetric, and antiphase Turing patterns in a model system with two identical coupled layers, *Phys. Rev. E*, **69** (2004), 026211. https://doi.org/10.1103/PhysRevE.69.026211
16. Z. Wang, L. Duan, Q. Cao, Multi-stability involved mixed bursting within the coupled pre-Bötzinger complex neurons, *Chin. Phys. B*, **27** (2018), 070502. https://doi.org/10.1088/1674-1056/27/7/070502
17. L. Duan, J. Liu, X. Chen, P. Xiao, Y. Zhao, Dynamics of in-phase and anti-phase bursting in the coupled pre-Bötzinger complex cells, *Cogn. Neurodyn.*, **11** (2017), 91–97 https://doi.org/10.1007/s11571-016-9411-3
18. Y. Zhao, M. Liu, Y. Zhao, L. Duan, Dynamics of mixed bursting in coupled pre-Bötzinger complex, *Acta Phys. Sinca*, **70** (2021), 120501. https://doi.org/10.7498/aps.70.20210093
19. X. Mao, W. Ding, X. Zhou, Complexity in time-delay networks of multiple interacting neural groups, *Electron. Res. Archive*, **29** (2021), 2973–2985. https://doi.org/10.3934/era.2021022
20. Q. Wen, S. Liu, B. Lu, Firing patterns and bifurcation analysis of neurons under electromagnetic induction, *Electron. Res. Archive*, **29** (2021), 3205–3226. https://doi.org/10.3934/era.2021034
21. X. Wang, H. Gu, B. Lu, Big homoclinic orbit bifurcation underlying post-inhibitory rebound spike and a novel threshold curve of a neuron, *Electron. Res. Archive*, **29** (2021), 2987–3015. https://doi.org/10.3934/era.2021023

22. C. Park, J. E. Rubin, Cooperation of intrinsic bursting and calcium oscillations underlying activity patterns of model pre-Bötzinger complex neurons, *J. Comput. Neurosci.*, **34** (2013), 345–366. https://doi.org/10.1007/s10827-012-0425-5

23. E. M. Izhikevich, Neural excitability, spiking and bursting, *Int. J. Bifurcat. Chaos*, **10** (2000), 1171–1266. https://doi.org/10.1142/S0218127400000840

AIMS Press